Validation of Aeromechanics Predictions for a Full 3-D Structural Analysis Model of the Tilt Rotor Aeroacoustic Model (TRAM) Proprotor

William Staruk
Ph.D. Candidate

Inderjit Chopra
Alfred Gessow Professor
Distinguished Professor

Anubhav Datta
Associate Professor

Buvana Jayaraman
Science and Technology Corporation

Alfred Gessow Rotorcraft Center
University of Maryland
College Park, MD
USA

U. S. Army Aeroflightdynamics Directorate
Ames Research Center
Moffett Field, CA
USA

ABSTRACT

This paper predicts and validates performance, airloads, and structural loads from an Integrated 3-D analysis of the NASA Tilt Rotor Aeroacoustic Model (TRAM). The analysis couples CAD-based 3-D computational structural dynamics with Reynolds-averaged Navier-Stokes (RANS) computational fluid dynamics (CFD). The use of 3-D structural modeling represents an advancement over the current state of the art in rotorcraft aeromechanics and the work presented here is the first application of this method to a real rotor. Furthermore, it is the first coupled CFD/Comprehensive Analysis of a tilting proprotor and opens the opportunity for fundamental understanding of the dynamic loads and stresses in conversion flight, which are critical to the design of advanced proprotors. Airloads and structural loads predictions are compared to experimental data at two test conditions, low thrust and high thrust, in edgewise flight at a 0.15 advance ratio. Airloads predictions show an over-prediction of steady normal force, but harmonics and the waveform are accurately captured. In the absence of direct strain measurements, experimentally measured blade loads must be used for validation. To this end, a method for extracting beam-like structural loads from the 3-D analysis is developed and verified using an analytical test case. When applied to TRAM, predictions show discrepancies in 3/rev and 2/rev harmonics for flap and lag bending, respectively, at high thrust. The torsion moments are qualitatively well predicted, showing significant high frequency content. Discrepancies in structural loads may be due to a lack of accurate composite material properties. To evaluate the extent of structural differences, sectional stiffness properties are extracted from the 3-D model and compared to experimental measurements, revealing an over-prediction of chordwise bending stiffness. The detailed 3-D bending stress fields are studied at several azimuths for blade cross-sections and the hub components, revealing localized stress patterns with lower stresses on the advancing side and higher stresses on the retreating.

1. NOMENCLATURE

a	speed of sound
A	rotor area
c	local chord
$c_n M^2$	normal force per unit span $/\ 1/2\rho a^2 c$
C_P	rotor power coefficient, $P/\rho(\Omega R)^3 A$
C_T	rotor thrust coefficient, $T/\rho(\Omega R)^2 A$ (shaft axes)
C_X	rotor propulsive force coefficient, $X/\rho(\Omega R)^2 A$
EI	bending stiffness
F_x	force in the global x-direction (extension)
GJ_x	torsional stiffness about the global x-axis
M_x	moment about the global x-axis (torsion)
M_y	moment about the global y-axis (flap)
M_z	moment about the global z-axis (lag)
P	rotor power
r	rotor radial station
T	air temperature
v	deflection in the global y-direction (lag)
V	wind tunnel velocity
w	deflection in the global z-direction (flap)
X	rotor propulsive force (wind axes, positive forward)
α_c	shaft angle of attack, corrected
α_s	shaft angle of attack, wind tunnel measurement
$\Delta\alpha$	shaft angle correction
β_{1c}	longitudinal blade flap angle
β_{1s}	lateral blade flap angle
δ	wind tunnel wall correction constant
θ	blade pitch angle
μ	rotor advance ratio $V/\omega R$
ρ	air density
σ	rotor solidity (0.105 for tram)
σ_{11}	axial/bending stress
σ_{12}	shear stress
ψ	blade azimuth angle (0° is downstream)
Ω	rotor rotation speed

2. INTRODUCTION

This paper presents performance, airloads, structural loads, and stress predictions generated by coupling a full 3-D finite element/multibody analysis solver with a Reynolds-averaged Navier-Stokes (RANS) solver for the NASA Tilt Rotor Aeroacoustic Model. The solvers used are X3D for computational structural dynamics (CSD)

and HPCMP CREATE™ – AV Helios [1] for computational fluid dynamics (CFD). The model was developed using a suite of 3-D structural modeling tools, including CATIA for geometry and Cubit for finite element analysis (FEA) meshing.

2.1. Background and Motivation

There is a large body of aerodynamic work devoted to tiltrotor performance and flow field predictions in hover – from early pioneering work in the 1990s (see [2, 3], for example) to more recent RANS simulations since 2000 (see [4, 5, 6], for example). Aeroelastic coupling is not important in hover, so no structural modeling was required for these studies. There is no gimbal motion in hover and the trim solution is trivial and almost always left out; a measured collective is prescribed instead.

Tiltrotor aeroelasticity research has largely been devoted to whirl flutter in cruise – from early pioneering work (see [7, 8, 9], for example) to more recent studies since 2000 (see [10, 11, 12], for example). The rotor induced inflow is not important in cruise, so high fidelity aerodynamic modeling was not needed for these studies. The wake is washed out by high cruise speed and the trajectory is trivial and mostly never calculated; a uniform inflow assumption typically suffices.

This separation breaks down in the conversion corridor where the tiltrotor encounters edgewise flow and works more similarly to a helicopter rotor, except a proprotor will encounter very high oscillatory and vibratory loads in this regime due to its stiff blades. The fundamental understanding and accurate prediction of these structural loads are essential for the design of future light weight tiltrotors.

There have only been limited attempts at predicting loads in the conversion regime. This is partly due to a lack of test data and partly due to the complexity of the physics, which require a detailed analysis. A proprotor wake is complex; characterized by stall delay, inboard vortex sheet development, outboard trailer consolidation, and negative lift roll-up near the tip – unique phenomena that require extensive semi-empirical corrections to a helicopter lifting-line analysis. In addition to aerodynamic complexities, proprotors are challenging to analyze structurally. Blades and hubs encompass spanwise discontinuities and many 3-D flexible parts near the root that are connected along multiple load paths through multiple joints. Such a structure is difficult to collapse neatly into equivalent boundary conditions for a conventional beam-type analysis.

Early works by Bilger et al. [13] and Totah and Madden [14] presented simplified calculations that ignored these complexities. The most comprehensive analysis thus far was carried out by Johnson [15, 16] who used systematic validation with TRAM experimental data to establish the important corrections required, for both lifting-line aerodynamics and beam structural dynamics. His study revealed two fundamental barriers in basic understanding and accurate predictions: 1) the advancing blade wake loading was difficult to predict consistently; corrections that improved airloads prediction deteriorated performance prediction and vice versa, and 2) the root end conditions were difficult to idealize; deflection and rap tests suggested different corrections and none produced rotating lag frequencies that seemed acceptable, so ad hoc corrections were still needed. This state of the art is not adequate for the design of new advanced rotors. The objectives of this research are to break these barriers systematically and advance the state of the art.

Since Johnson [16], a major milestone in aeromechanics has been the establishment of CFD/comprehensive analysis (CA) coupling, which effectively replaces lifting line aerodynamics with RANS [17, 18]. The first objective of this work is to bring this advancement to bear for the tiltrotor problem and resolve barrier 1. Since its debut in CFD/CA, RANS has undergone major advancements (including adaptive mesh refinement, structured/unstructured multi-solvers, algorithms for massive scalability, and new and innovative meshing), but CSD has continued to use the same beam-level structural models. Thus the second, and primary, objective of this paper is to provide a leap in CFD/CA by integrating full 3-D structural dynamics and resolve barrier 2. Three dimensional structures refer to 3-D solid elements (and multibody joints) that solve the full 3-D governing equations in the structural domain with no reduced order approximation. They couple with RANS through a 3-D interface. The trim solution is obtained the same way as current generation CFD/CA. This level of modeling is denoted by Integrated 3-D in this paper.

2.2. Outline of the Paper

Following this introduction, Section 3 discusses the methodology employed. It describes the solvers used (X3D and Helios) and the techniques applied to extract sectional stiffness properties and sectional blade loads from 3-D structural analysis models. Section 4 contains details on the model, introducing the TRAM rotor, discussing the development of the 3-D model, and describing the CFD model and coupling. Section 5 presents the results of this work, including performance using three aerodynamics models, airloads calculated by RANS, and blade loads calculated using X3D. Detailed 3-D stresses are also presented and discussed. Finally, Section 6 offers some conclusions and recommendations for future work.

3. METHODOLOGY

3.1. The X3D Solver

For 3-D structural dynamics, the X3D solver developed by Datta is used [19]. Initial research with X3D focused

on the feasibility of the method and developing the toolsets and methodologies to create the required 3-D rotor models using idealized or notional rotor geometry [20, 21, 22]. After these studies proved the capabilities of the solver, a structural analysis model for the NASA TRAM proprotor was developed [23] and performance and airloads predictions with low order aerodynamic models were presented [24]. This paper is the first attempt to couple X3D with RANS for a fully Integrated 3-D aeromechanics analysis.

X3D utilizes a multibody analysis framework in which flexible components are analyzed using full 3-D FEA. The finite element analysis is parallelizable through the use of scalable domain decomposition. Kinematic couplings are simulated by the multibody analysis of the solver and 3-D stresses and strains are recovered from the FEA. The X3D solver, in addition to structural dynamics, has simple built-in aerodynamics, intended to provide the minimum capability required to couple with CFD. Full details of the solver and its integration with rotor aeromechanics are provided by Datta [19].

The structural analysis performed for this paper was carried out on a single processor. Although the solver is parallelizable, and scalability has been demonstrated on simplified geometries [20], generalized domain decomposition schemes have not yet been developed for more advanced rotor meshes. Hence, coarse meshes are used here for computational efficiency.

3.2. Helios

The Helios CFD solver is part of the HPCMP CREATE™ – AV software program. It is an integrated capability consisting of an unstructured, node-centered, implicit RANS (Spalart-Allmaras turbulence) near-body solver; an overset Cartesian, explicit, Euler off-body solver; and an implicit hole-cutting based domain connectivity algorithm. A description of its general architecture can be found in [1]; validation of its aerodynamic and CFD/CSD capabilities can be found in [25].

3.3. Sectional Stiffness from 3-D

Although sectional properties are not needed for 3-D CSD analysis, comparisons to experimental measurements are useful for first order verification of the model geometry and material inputs. An earlier paper by the authors [24] presented a method for extracting equivalent beam-like sectional properties (bending stiffness *EI* and torsional stiffness *GJ*) from CAD-based 3-D structural analysis models using X3D. That simple method uses the equivalent 1-D sectional deformations output by X3D to determine the bending slope or rate of twist of a beam due to a tip load and thereby calculates *EI* or *GJ* in the same manner as experimental stiffness measurements. This method was validated for simple beams, including those with tapered or discontinuous stepped geometry. However, it did not consider the flap/lag bending coupling that arises from pre-twisted beams.

For twisted beams, there is an inherent structural coupling between the flap and lag degrees of freedom that results from the principal axes of the beam not being aligned with the global reference axes. Based on analytical deformations of a twisted beam [26], the method for extracting sectional bending stiffness can be modified for a structurally coupled blade. Instead of considering a single flap stiffness and lag stiffness, a coupled formulation of the Euler-Bernoulli theory can be expressed in the global reference fame, in which the bending stiffness is a 2-by-2 matrix. This method produces direct stiffness about the global axes, EI_{zz} and EI_{yy}, as well as the stiffness products EI_{yz} and EI_{zy} which describe flap/lag coupling.

Alternatively, the sectional beam stiffness can be defined in the local coordinate frame, along the principal axes of the cross-section: EI_{cc} about the chordwise axis and EI_{nn} about the normal axis. This is the same as the original uncoupled method, but requires rotation of the flap and lag bending slopes and the internal bending moments into the local coordinate frame. It is only possible if the rotation angle from the global reference frame to the principal axes of the cross-section is known.

For validation of both the global and local forms of the sectional property extraction method, a twisted box beam is considered. Figure 1 shows the beam, which goes through 90° of twist from its root to its tip. This beam was created using corner helical guide curves, creating a constant-width, linearly twisted beam (the importance of properly describing the width and twist of a beam is discussed in reference [27]). Figure 2 shows that both the global and local extracted sectional bending stiffnesses match the geometrically calculated analytical values. Torsion prediction is not affected by pre-twist in beams, and validation of GJ extraction can be found in [24].

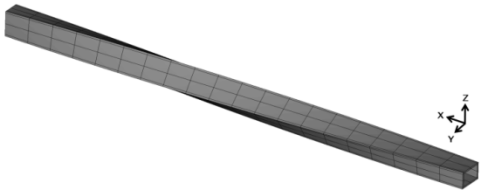

Figure 1. Drawing of the twisted beam mesh

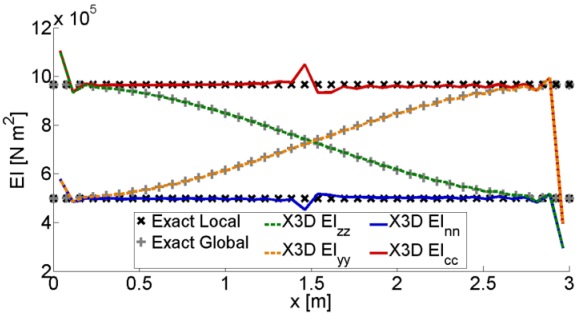

Figure 2. Bending stiffness of the twisted box beam calculated using X3D

3.4. Sectional Blade Loads from 3-D

While X3D generates detailed 3-D stresses and strains over the entire rotor, experiments provide structural loads calibrated in terms of sectional bending and torsion moments. There is no direct way to compare these sectional loads to the results from X3D other than integrating sectional stresses as a post processing step; a more elegant method is desired to validate the 3-D predictions.

One method is to break a mesh at the location where the loads are desired, and place a stiff joint between the segments. This joint can act as a load sensor, measuring net blade loads. However, this is an approximate method as it constrains the deformations of the section artificially and the joints have an impact on the dynamics of the system. Instead, a method has been developed to use the 3-D strain field to extract sectional blade loads. Analogous to experimental calibration of strain gauges embedded in the blade surface, this method calibrates strains calculated by X3D against applied tip loads as a pre-processing step. The calibration can then be used to determine the sectional loads from any strain condition.

First, four nodes are identified, one each on the top, the bottom, the leading edge, and the trailing edge of the cross-section, as indicated in Figure 3 for a twisted beam.

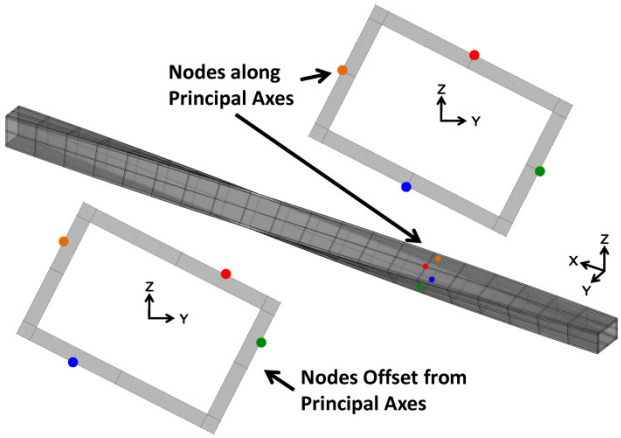

Figure 3. Twisted beam with nodes identified for calculating sectional loads at 0.3R

Tip loads (F_x, M_x, M_y, M_z) of varying magnitude are applied in X3D one at a time, and the strains generated by each loading at the four cross-sectional nodes are identified. The strains are then grouped into four pairs:

$$(1) \qquad \begin{bmatrix} EX \\ ET \\ EF \\ EL \end{bmatrix} \equiv \begin{bmatrix} \epsilon_{11_{Top}} + \epsilon_{11_{Bottom}} \\ \epsilon_{12_{Top}} - \epsilon_{12_{Bottom}} \\ \epsilon_{11_{Top}} - \epsilon_{11_{Bottom}} \\ \epsilon_{11_{Leading\ Edge}} - \epsilon_{11_{Trailing\ Edge}} \end{bmatrix},$$

where EX, ET, EF, and EL represent the extension, torsion, flapwise, and lagwise strain pairs, respectively. By taking the sum and differences in this manner, the effects of any one load on the other is minimized. However, there can still be coupling between loads and uncorrelated strain pairs due to structural coupling or the nodes not being on the principal axes (bottom left inset of Figure 3). For these reasons, the calibration takes the form of a Jacobian matrix. Each entry of the Jacobian is the partial derivative of each of the four strain pairs (EX, ET, EF, and EL) with respect to the four sectional tip loadings (F_x, M_x, M_y, M_z). The Jacobian correlates the known sectional loads to the measured strain; the system can then be solved (inverting the Jacobian) to calculate unknown sectional blade loads from an arbitrary strain field.

For verification of the method, the twisted beam in Figure 3 is subjected to a combined tip loading with steady axial force and torsion moment plus harmonic flap and lag bending moments applied to the tip. Two models have been considered, one as depicted in the figure, and another split at the same radial location (30% R) with a stiff joint used as a load sensor. Figure 4 shows that the dynamic sectional loads are recovered exactly using the strain extraction method, even when the nodes are offset from the principal axes. If the full Jacobian is not used, there will be contamination of the combined tip loading result, and errors will appear in the predictions for twisted beams or beams with nodes not placed at the principal axes.

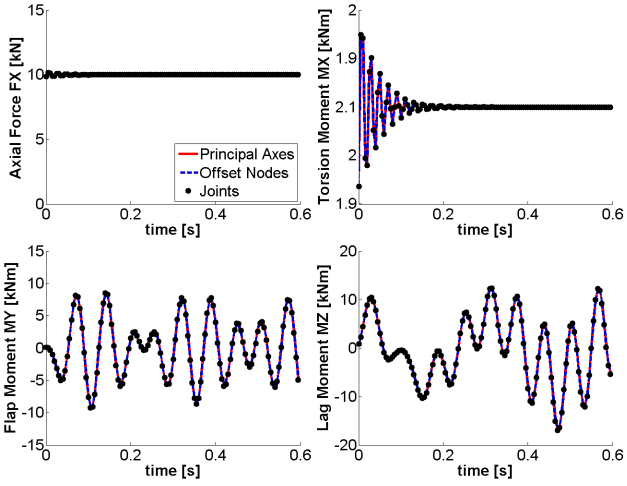

Figure 4. Dynamic sectional loads for a twisted beam

4. MODELING

4.1. The TRAM Rotor

The Tilt Rotor Aeroacoustic Model is a ¼-scale model of the V-22 rotor developed by NASA. The isolated rotor was tested at the German-Dutch Wind Tunnel (DNW) in the Netherlands [28]. The TRAM rotor is dynamically scaled to match the V-22 frequencies in the first flap, lag, and torsion modes. TRAM was chosen as the basis for this research because un-published details of its structural design and construction were made available by NASA Ames Research Center specifically for this task. TRAM

performance, airloads, and structural loads measurements were made available by NASA for validation, and comprehensive analysis results can be found in the literature [15].

The first step in the 3-D modeling procedure was developing a CAD model of TRAM in CATIA from the original engineering drawings (Figure 5). The rotor has three blades, each held in place by a grip that also serves as a pitchcase for transferring torque from the pitch link. The pitchcase is connected to a flexbeam, which it surrounds, by two sets of centering bearings: one outboard of the flexbeam and one inboard; thus the rotor has a dual load path. The flexbeam serves as the primary flapping hinge of the stiff-in-plane rotor, and is connected to the gimbaled hub at its root.

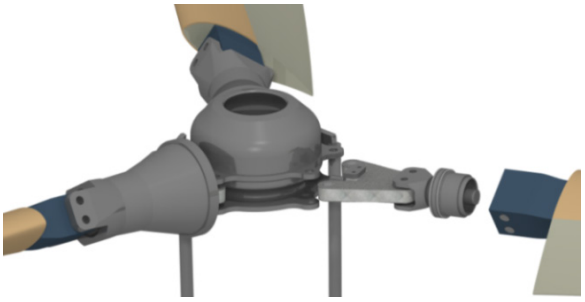

Figure 5. CAD model of the TRAM rotor developed for this research

4.2. TRAM 3-D Structural Analysis Model

Once the CAD model was completed, a structural analysis representation was developed (Figure 6), in which the method of modeling each rotor component (as a flexible part or a kinematic joint) was assigned. The blade, flexbeam, pitchcase, pitch horn, and pitch link were modeled as flexible parts (F) with full 3-D FEA. The bolts between the pitchcase and the blade, the outboard and inboard bearings and carriers, hub gimbal, and pitch link connections were modeled as joints (J).

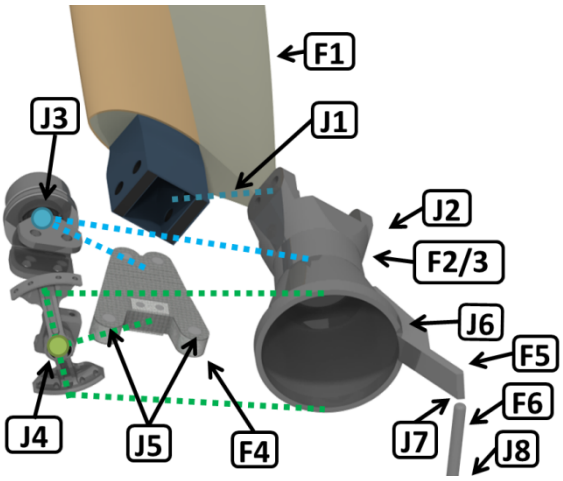

Figure 6. Schematic of the TRAM blade assembly structural analysis representation

Once part types had been assigned, the individual flexible parts within the rotor were meshed using Cubit, a mesh pre-processor created by Sandia National Laboratories [29]. Three meshes of the blade were created at various levels of fineness. Prior work [23] showed that the medium mesh gave satisfactory results at a faster solution time than the fine mesh, and only results for the medium mesh are presented in this paper. The individual meshes were assembled to form a final structural analysis model of the TRAM proprotor blade, depicted in Figure 7.

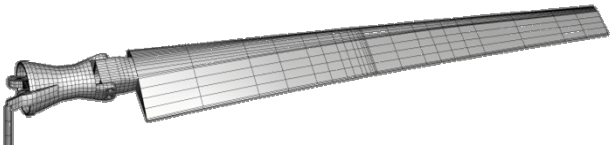

Figure 7. The TRAM blade structural analysis model

In order to represent composite materials without driving the degrees of freedom too high to solve quickly, a homogenization method was employed. It finds an effective modulus matrix for a composite laminate composed of multiple plies of orthotropic material. Material modeling for the TRAM rotor has proven to be a great source of difficulty during this research effort due to the dearth of available material specifications. Because of this, material properties (such as shear modulus and Poisson ratio) typical of the composites used in the rotor were obtained from a variety of sources. The development of the structural analysis model is discussed in greater detail in [23] and [24].

The total problem size was 43.8 thousand degrees of freedom: 1,709 elements, eight joints, about 30 different materials, and two hub load sensors (one at the gimbal and one below the pitch link). A Generalized-α scheme, executed in a simple Newmark-β mode, with an azimuth resolution of 7.5° was used. Trim is controlled via collective and cyclic inputs at the bottom of the pitch link, which is connected to a vertical slider joint (J8, Figure 6).

4.3. Aerodynamics Modeling

X3D aeromechanics results were calculated using multiple aerodynamics models, including linear inflow and free-vortex wake [24]. For CFD results, Helios was used. It uses a dual mesh paradigm: here unstructured RANS (NSU3D) is used as the near-body solver and Cartesian Euler is used as the off-body solver. The TRAM CFD mesh used (Figure 8) is a fine mesh reported recently for hover predictions by Wissink et al. [6] (Table 4, Fine (no subset) and Fig 7(b) for near-body and Table 9, No subset-7L for off-body) containing 9.27 million grid points for near body and 26 million for off-body. An azimuth resolution of 0.25° was used (implicit near-body, explicit off-body; see [25] for details). The simulations were performed on 128 cores.

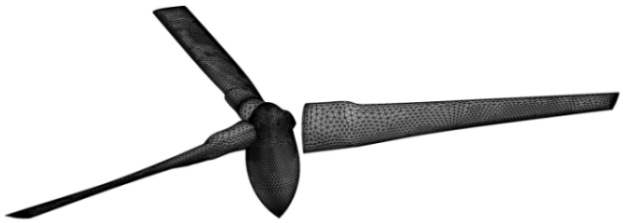

Figure 8. CFD mesh of the TRAM rotor

The fluid structure interface consisted of 55.6 thousand on-surface nodes of the near-body CFD mesh and 391 surface elements of the structural solver mesh. X3D provides an interface for external CFD software coupling. The interface is available both as a file-based input/output capability as well as a Python-based module with associated drivers. The Python-based module is part of the Helios framework. All current generation rotorcraft CFD software (including Helios) use a 1-D beam-like interface to exchange deformations and airloads. Therefore, even if inexact in the context of 3-D, such an interface (defined as level-I, see [19] for details) is used here; it is the only interface that allows CFD/CA coupling with no changes in the CFD domain. To pass structural deflections to CFD, the 3-D blade deformations are reduced to a 1-D beam like description about 1/4-chord (12 harmonics transferred to CFD). To return airloads to X3D, the 3-D surface traction is collapsed into segmental (dimensional) normal and chordwise forces and 1/4-chord pitching moment and distributed over all surface nodes at each azimuth.

The solution then proceeds as per the usual delta coupling procedure. A total of eight iterations were carried out with CFD airloads exchanged over 1, 1, and six sets of 1/3 revolutions. The simulation time was around 3-4 days in total, of which X3D's share was 10 hours: about two hours for the baseline solution and about one hour on an average for each subsequent trim solution.

5. AEROMECHANICS PREDICTIONS

5.1. Test Conditions

The predictions shown in this paper are compared to experimental test data for TRAM in the DNW wind tunnel. All results presented are for edgewise flight at an advance ratio (μ) of 0.15, with the trim targets being thrust and first harmonic gimbal flapping. Two thrust conditions are considered: high thrust, with a 0.128 nominal normalized thrust coefficient (C_T/σ), and low thrust with 0.089 nominal C_T/σ.

Performance data for the linear inflow and free-vortex wake models are provided at a range of shaft angles from -10° (toward the flow) to 10° (away from the flow). The flight condition inputs for X3D matched those at which the experimental data were taken in the DNW wind tunnel, provided in Table 1. Due to the high computational time required to complete a trimmed solution, CFD results are only presented at a -2° nominal shaft tilt angle for each thrust case (Run 605 point 122 and run 605 point 177, highlighted in Table 1).

Table 1. Test conditions for the TRAM rotor, μ = 0.15 (CFD test cases in bold)

High Thrust Test Cases, μ = 0.15						
Run	607	605	**605**	605	603	603
Point	68	252	**177**	68	13	39
α_s (°)	-9.98	-5.99	**-2.10**	1.93	5.95	10.03
α_c (°)	-11.32	-7.34	**-3.43**	0.59	4.60	8.69
T (°C)	16.61	18.13	**17.62**	16.48	14.94	15.87
ρ (kg/m^3)	1.198	1.198	**1.200**	1.207	1.220	1.216
V (m/s)	32.19	32.12	**32.07**	32.32	32.19	32.13
Ω (rad/s)	147.6	147.6	**147.6**	147.6	147.8	147.8
C_T/σ	0.127	0.126	**0.124**	0.127	0.127	0.126
β_{1c}	0.06	0.26	**0.09**	0.10	0.22	0.23
β_{1s}	-0.03	0.01	**0.00**	0.09	0.31	0.26
Low Thrust Test Cases, μ = 0.15						
Run	607	605	**605**	605	603	603
Point	13	231	**122**	10	7	72
α_s (°)	-9.99	-6.00	**-2.03**	1.99	5.94	9.95
α_c (°)	-10.92	-6.94	**-2.97**	1.04	4.98	9.02
T (°C)	15.3	17.9	**17.0**	15.1	14.4	16.4
ρ (kg/m^3)	1.203	1.199	**1.204**	1.213	1.223	1.214
V (m/s)	32.26	32.19	**32.25**	32.11	31.99	32.22
Ω (rad/s)	147.6	147.6	**147.6**	147.6	147.7	147.7
C_T/σ	0.088	0.088	**0.088**	0.089	0.088	0.089
β_{1c}	-0.04	0.07	**0.09**	0.03	-0.14	-0.30
β_{1s}	-0.08	-0.09	**0.16**	0.10	-0.13	-0.33

The wind tunnel wall correction factor added to the measured wind tunnel shaft angle (α_s) to generate α_c was:

$$\Delta\alpha = \delta\, 0.02881 \frac{C_L/\sigma}{\mu^2}, \quad (2)$$

where $\Delta\alpha$ is the shaft correction, δ is the wall correction constant equal to -0.147 for TRAM in the DNW wind tunnel, μ is the ratio of tunnel velocity to rotor tip speed, and C_L/σ is the rotor lift coefficient, which is approximately equal to C_T/σ [15].

5.2. Rotor Frequencies

The rotor frequencies in vacuum for the TRAM model are shown in Figure 9. The results from X3D are compared to beam-based calculations from CAMRAD II and non-rotating rap test frequencies [15]. The lower modes are well matched, though there are discrepancies from both CAMRAD and the non-rotating data for higher modes.

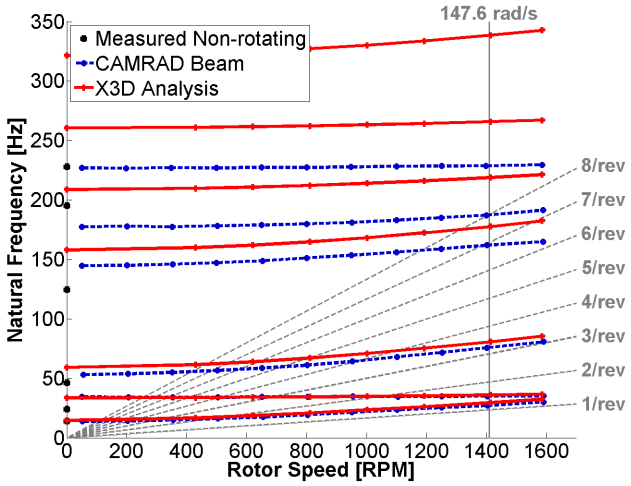

Figure 9. Rotating frequencies for the TRAM structural analysis model, gimbal locked

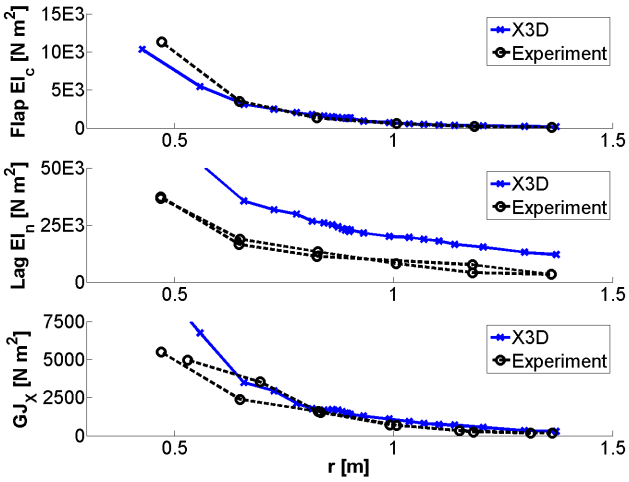

Figure 10. TRAM blade sectional properties: flap and chordwise bending and torsional stiffness

Differences between CAMRAD and X3D analysis are due to the nature of the structural models and the inputs they require. The beam-based analysis uses an equivalent root spring with an empirically determined stiffness to represent all of the root components of the TRAM blade, whereas X3D models each part directly. This is not to say X3D is without some tuning; joint stiffnesses were not available and had to be adjusted to match the first lag frequency [24].

Differences in the higher mode frequencies can be attributed to discrepancies between the beam model and the 3-D model. These discrepancies can be seen by comparing the sectional properties of the 3-D TRAM structural analysis mode to those used by CAMRAD. Figure 10 shows the TRAM sectional properties (in the local frame) extracted using X3D compared to experimental measurements, which were the source of the inputs for the beam-based CAMRAD II analysis [15]. Note that some measurements have multiple experimental lines; these are due to differences in individual blades, and cover the range of variation in measured values. The structural analysis model well matches flapwise bending stiffness (EI_c) and of torsional stiffness (GJ_x), but chordwise bending stiffness (EI_n) is over-predicted by a factor of approximately two. The error in chordwise stiffness is believed to be the source of modal frequency discrepancies, and is suspected to be due to errors in the material properties used, as discussed in [24].

5.3. Performance

Performance predictions with linear inflow, free-vortex wake, and CFD aerodynamics are plotted versus wind tunnel shaft angle and compared to experimental data in Figure 11 (power) and Figure 12 (propulsive force). Linear inflow consistently under-predicts the power required (C_P/σ) and over-predicts the propulsive force (C_X/σ). Using a free-vortex wake model improves the performance predictions. RANS offers equally good power predictions as free-vortex wake at both thrust levels for the one shaft tilt case considered, but fails to predict the propulsive force accurately.

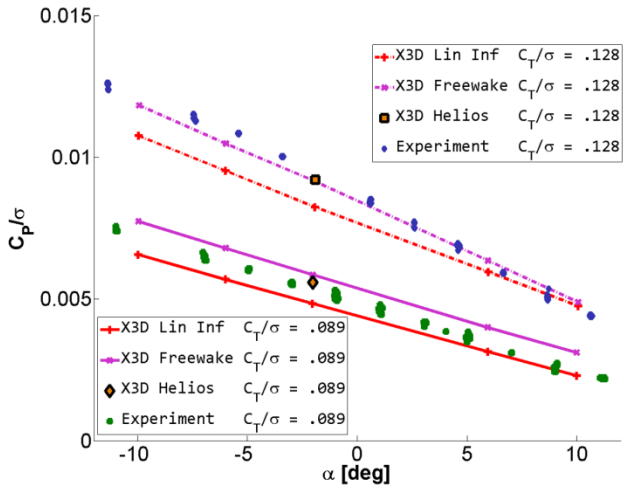

Figure 11. Power for the TRAM rotor in edgewise flight, μ = 0.15

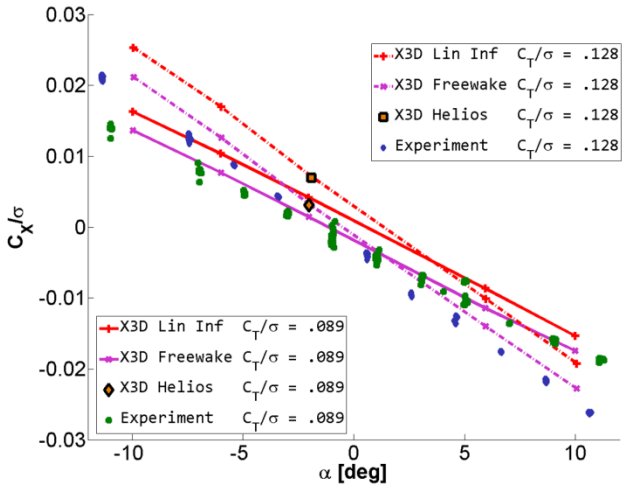

Figure 12. Propulsive force for the TRAM rotor in edgewise flight, $\mu = 0.15$

5.4. Airloads

Figure 13 compares the mean removed experimentally measured and RANS calculated airloads near the tip of the blade (90% *R*). Only values for sectional lift are shown, as those experimental data were previously published by NASA [15]. The RANS model does a good job of capturing the airloads on the rotor at every azimuth. Results are also presented further inboard (72% *R*) in Figure 14. Once again, the predictions show very good correlation with the measured airloads.

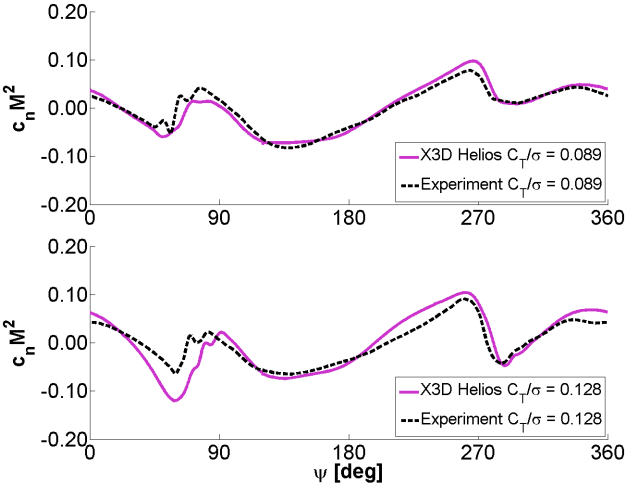

Figure 13. Experimental and RANS mean removed normal force airloads for wind tunnel trim of the TRAM rotor, $\mu = 0.15$, $r/R = 0.90$

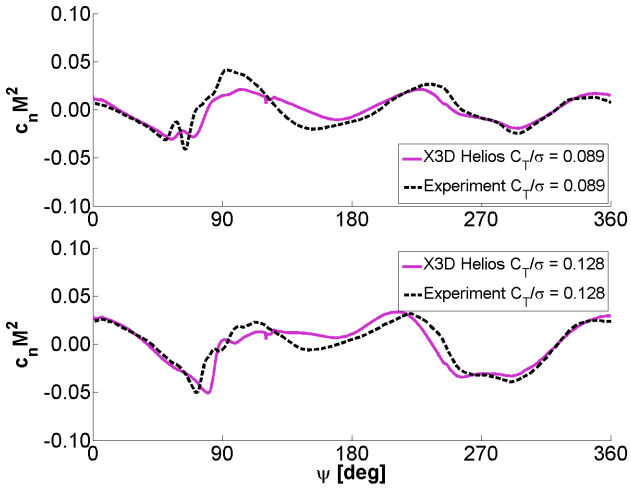

Figure 14. Experimental and RANS mean removed normal force airloads for wind tunnel trim of the TRAM rotor, $\mu = 0.15$, $r/R = 0.72$

Figure 15 shows the wake of the high thrust case (Q-criterion iso-surfaces, |Q| = 1e-5) colored by vorticity. The airload impulses in the first and fourth quadrants are a direct result of interaction with the rolled up vortices from the preceding blades. Clearly the first one or two turns are the most crucial, as most of the vorticity seen in the far field has little or no impact. The center body (Figure 8) is important and appears to set the proper distribution of bound circulation; without it the airload predictions deteriorate dramatically.

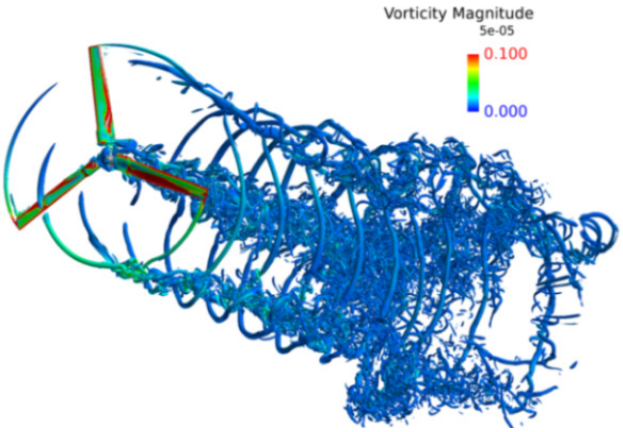

Figure 15. Vorticity of the rotor wake: high thrust condition (run 605 point 177)

Greater insight can be obtained by assessing the accuracy of harmonic components of the airloads along the blade span. Figure 16 presents the steady component of the sectional lift coefficient, which is over-predicted. The airload impulses generate all four dominant harmonics (1/rev to 4/rev for the 3-bladed rotor), as shown in Figure 17. All of the basic features are in place, including the differences between high and low thrust. The only discrepancy is an over-prediction of the 3/rev airloads outboard for the high thrust case. The reason behind this is not clear at present.

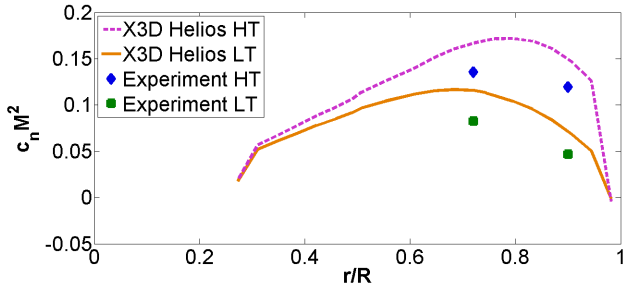

Figure 16. Steady component of the TRAM sectional normal force along the blade

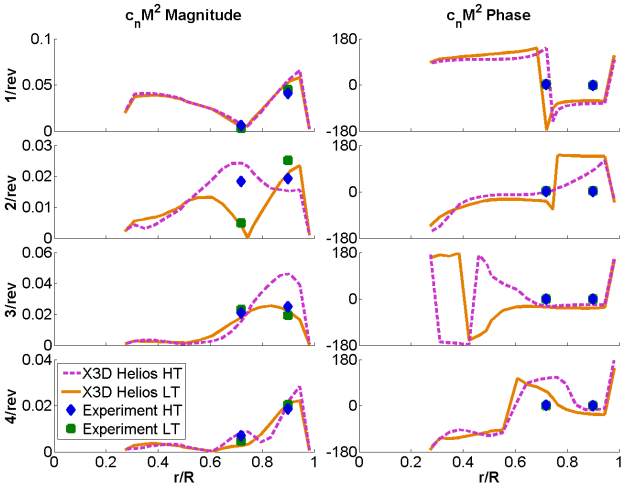

Figure 17. Harmonic components (1/rev to 4/rev) of the TRAM sectional normal force along the blade, magnitude and phase angle

5.5. Blade Loads

Blade loads for the TRAM rotor were calculated at three spanwise stations, identified by orange arrows in Figure 18, using the strain extraction method. They are compared to experimental values available at the radial locations marked by green lines in the figure. The first and third strain gauge locations (23% R and 50% R) were used to experimentally measure flap and lag bending moments, and the second (43% R) was used for torsion. As can be seen in the figure, there is a mismatch between the radial position of mesh nodes and the third strain gauge location: the X3D section is at 47.8% of the rotor radius, whereas the experimental strain gauge to which it is compared was positioned at 50.0% radius. The other two strain gauge locations match the mesh well.

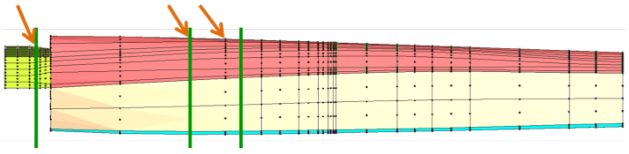

Figure 18. Image of the TRAM mesh identifying experimental strain gauge locations (green lines) and X3D strain cross-sections (orange arrows)

To verify the accuracy of strain based sectional loads for the TRAM blade, the rotor blade assembly was subjected to a dynamic load at the blade tip. Sectional loads were extracted for the innermost cross-section (23% R) and compared to the loads sensed at joint J1 (Figure 6) which connects the blade to its grip and is located just inboard of the cross-section.

The top subfigure of Figure 19 shows the dynamic flap bending moment at the blade root when the rotor is impulsively rotated up to the experimental test speed (147.6 rad/s), with no applied tip load. The strain-based sectional loads extraction method matches well with the flap bending moment sensed at joint J1; the same is true of the other blade loads (not shown). Blade loads were also well matched for a non-rotating blade undergoing dynamic tip loading (middle subfigure, Figure 19). Despite these results, the bottom subfigure of Figure 19 shows a steady offset in the flap bending moment when the blade is subjected to both rotation and a dynamic tip load. It is not clear why this occurs, but the dynamics seem to be well matched. The same phenomenon also occurred in lag, though axial force and torsional moment were correct. Steady offsets were also observed in the edgewise flight blade load results. For this reason, only mean removed blade loads are presented subsequently.

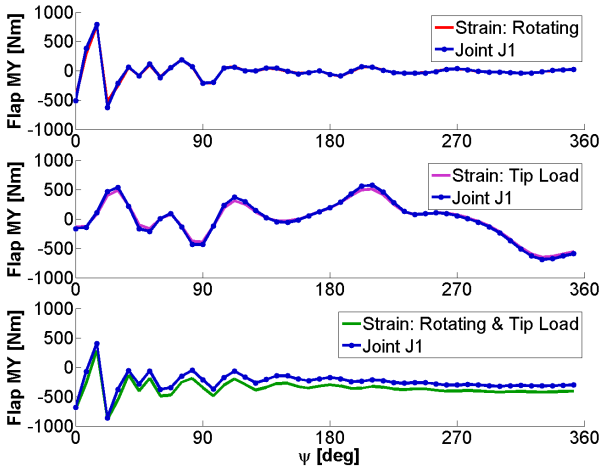

Figure 19. Dynamic TRAM flap bending moment, calculated using strain calibration and joint sensor

Figures 20, 21, and 22 show the sectional flap, lag, and torsion moments, respectively, calculated by X3D coupled with Helios for the high and low thrust edgewise flight cases (run 605 point 177 and run 605 point 122). Bending moments are plotted at 48% of the rotor radius for X3D results and 50% of radius for experimental results. Torsion moment is shown at 43% radius for both experimental and X3D results. The overall trends in flap are matched at low thrust with similar peak-to-peak loads, but at high thrust there is a considerable 3/rev moment which is missed by the analysis. This is despite the fact that 3/rev airloads were over-predicted in the airloads analysis (Figure 17). This might be due to a gimbal effect not being represented properly.

At both thrust levels, the overall trend in lag is picked up, though higher frequency content is not. At high thrust a large 2/rev component appears in the experiment but is missed by the analysis.

The experimentally measured torsion moments are characterized by considerable high frequency content, which is unsurprising because the first torsion mode frequency is on the order of 9/rev. The analysis shows the same qualitative behavior, with high frequency content and similar peak to peak loads. A high frequency spike in the fourth quadrant is not captured for the high thrust case.

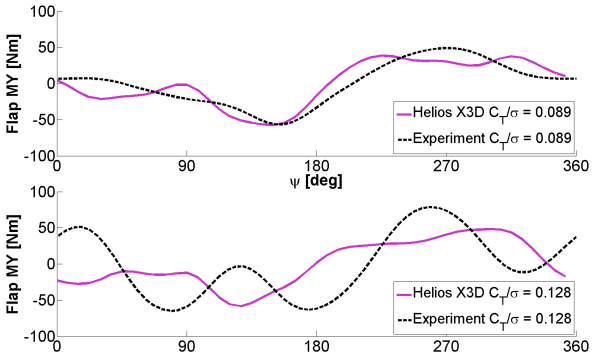

Figure 20. Flap bending moment, mean removed, $r = 0.48R$ for analysis, 0.50R for experiment

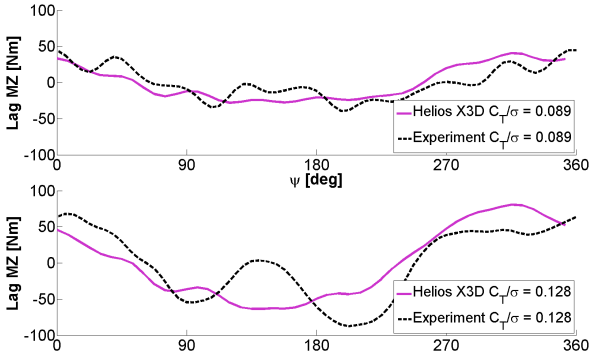

Figure 21. Lag bending moment, mean removed, $r = 0.48R$ for analysis, 0.50R for experiment

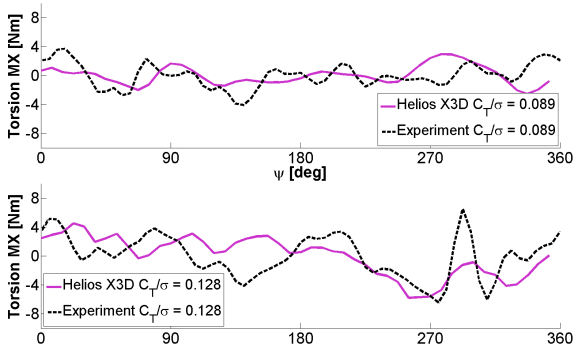

Figure 22. Torsion moment for the TRAM blade, mean removed, $r = 0.43R$

5.6. Three-Dimensional Stress Distribution

Figures 23 and 24 show the internal axial blade stresses for the high thrust and low thrust conditions, respectively, at 0°, 90°, 180°, and 270° azimuths. Figures 25 and 26 show the stresses at the root end of the blade for the high and low thrust cases, respectively, for the same four azimuth angles. Note that these figures are generated by breaking each 2nd order 27-noded hex element into eight 8-noded 1st order hex elements; as such this visualization may not represent some of the higher-order information which exists in the analysis. The plots shown here provide only a small sample of the data generated by X3D, which includes all six stresses and strains; a few brief observations are offered, but in depth analysis will be required.

Examination of the cross-sections (Figures 23 and 24) reveals that the blade spar takes most of the stress, as expected, but there appears to be some stress carried by the blade core and leading edge weight, most visible as a green area aft of the spar in the 0° high thrust case (Figure 23). However, this is due to interpolation of the high stress at the spar wall across the element by the linear interpolation used in the visualization.

For both thrust cases, the highest stresses occur from the retreating side around to 0° azimuth, which is consistent with flap and lag bending moment patterns. In both the high and low thrust cases, very high stresses can be observed in the blade spar (Figure 23d, inboard spar cross-section). These stresses appear higher than the blade materials can withstand, and as such cannot represent the TRAM blade as built. Close examination is required to determine whether this is due to over-prediction of the steady airloads, errors in the material modulus (a known issue with this structural analysis model), or something else.

Examining the stresses at the root end (Figure 25 and Figure 26) reveals that the flexbeam never experiences high stress. The pitchcase, on the other hand, experiences very high stress around the retreating side to 0° azimuth. The high loads may be an artifact of the material selection; aluminum was used in this structural analysis model, though the pitchcase in the wind tunnel model was switched later to titanium. It may also indicate improper load sharing between the pitchcase and the flexbeam, possibly indicating the importance of bearing joints whose exact properties are unknown.

6. CONCLUDING REMARKS

A 3-D rotor structural analysis solver (X3D) was coupled to a 3-D RANS CFD solver (Helios) for an Integrated 3-D CFD/CSD analysis of the TRAM proprotor. A means of calculating equivalent sectional properties for 3-D models of pre-twisted beams was presented and validated. A method for extracting equivalent sectional blade loads from 3-D FEA strain data was presented and verified

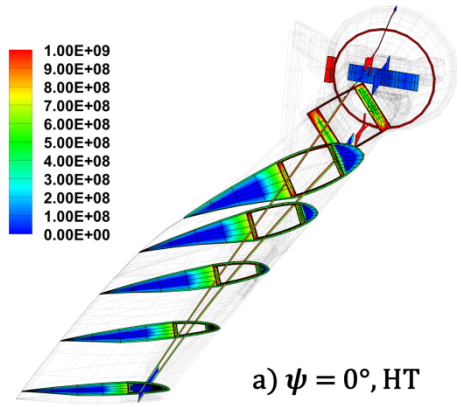

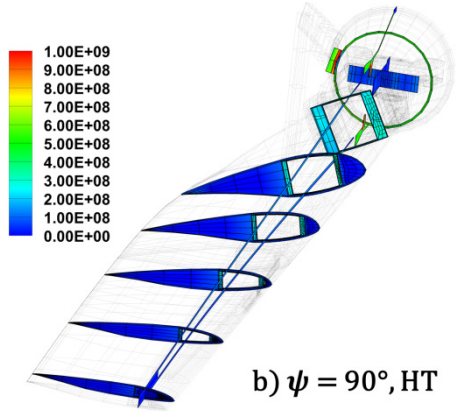

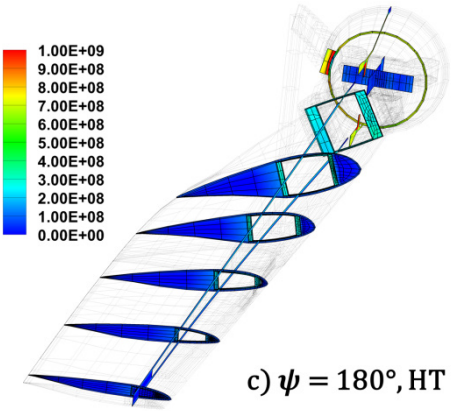

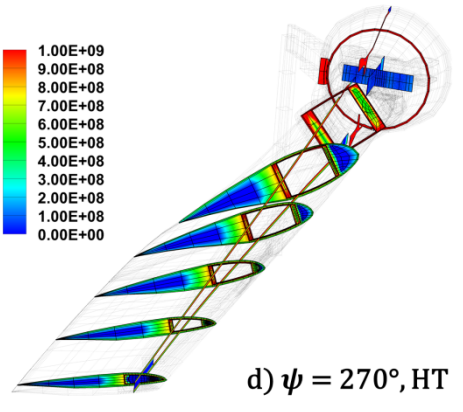

Figure 23. High thrust (HT) 605.177: Blade σ_{11} [N/m^2]

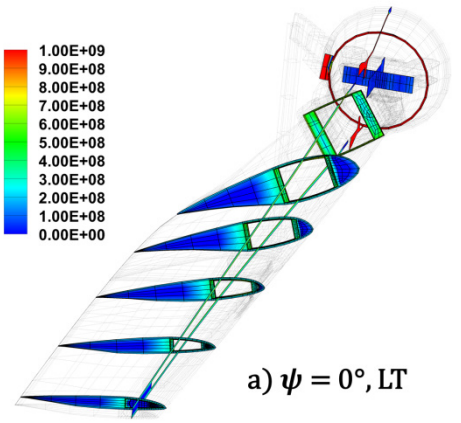

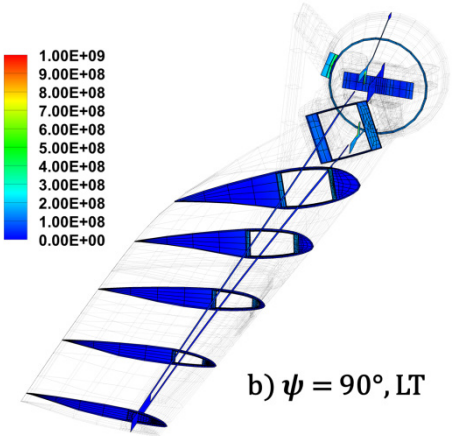

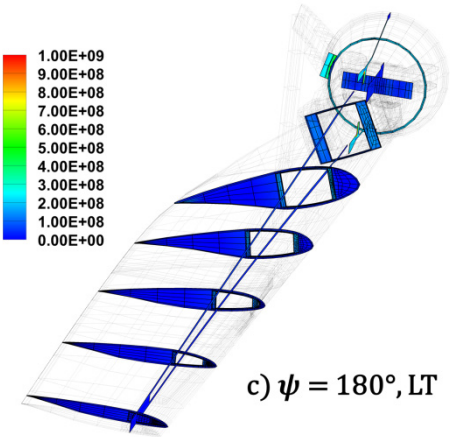

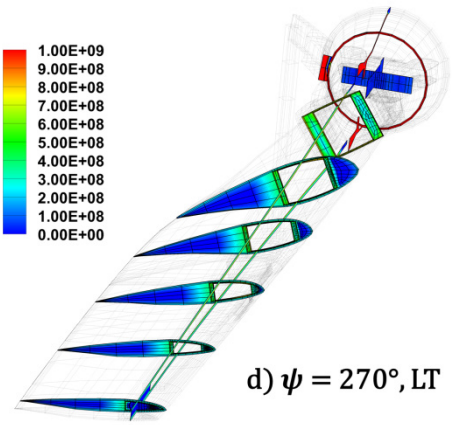

Figure 24. Low thrust (LT) 605.122: Blade σ_{11} [N/m^2]

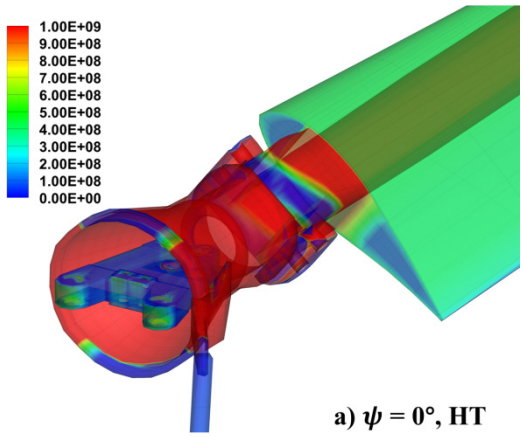

a) ψ = 0°, HT

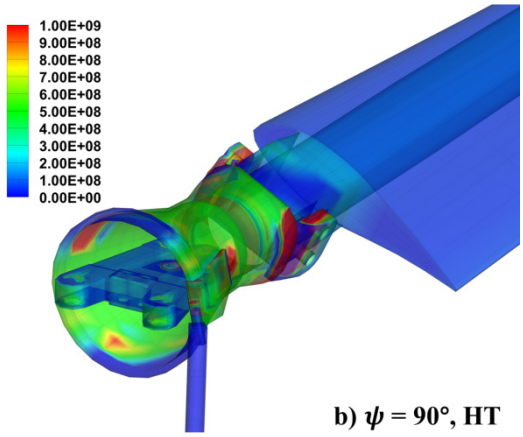

b) ψ = 90°, HT

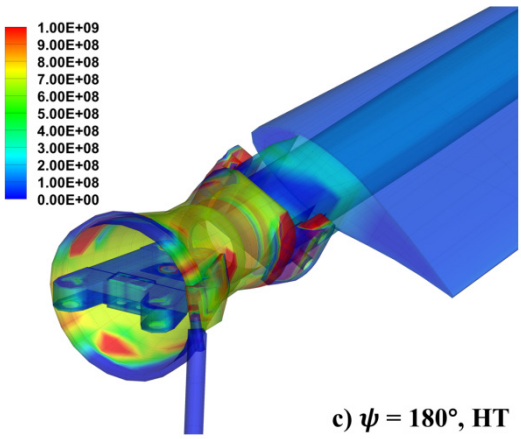

c) ψ = 180°, HT

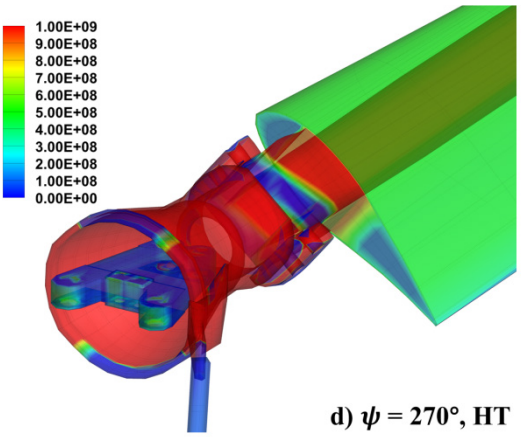

d) ψ = 270°, HT

Figure 25. High thrust (HT) 605.177: Root σ_{11} [N/m^2]

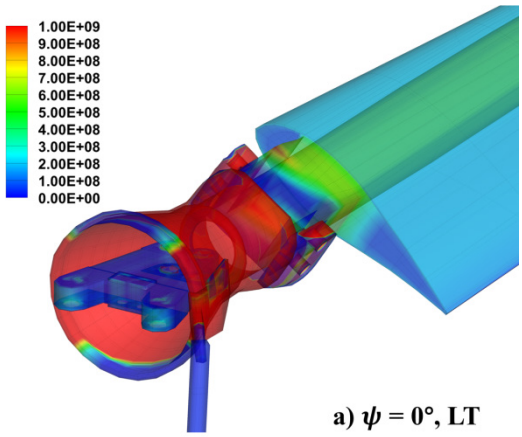

a) ψ = 0°, LT

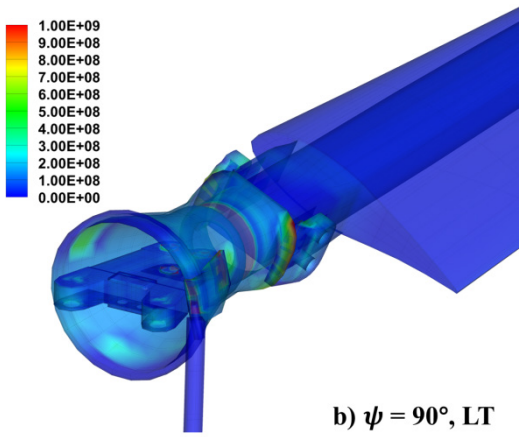

b) ψ = 90°, LT

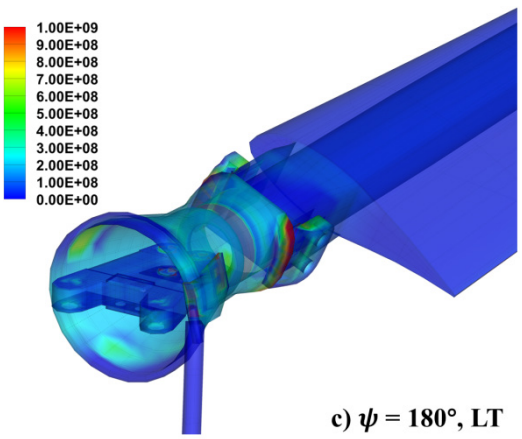

c) ψ = 180°, LT

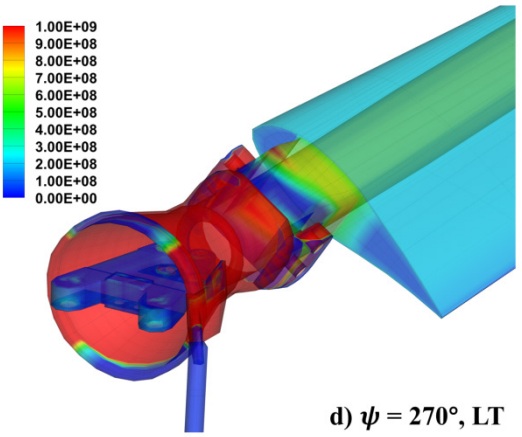

d) ψ = 270°, LT

Figure 26. Low thrust (LT) 605.122: Root σ_{11} [N/m^2]

using a simple twisted beam. Performance, airloads, and blade loads predictions for the TRAM rotor were compared to experimental measurements. Detailed stress plots from the coupled X3D/Helios analysis were shown, and some initial insight on the stress patterns was provided. From this work, the following conclusions can be made:

1. Performance predictions show that a free-vortex wake model performs better than linear inflow for both power and propulsive force. RANS provides an equally good power prediction, but over estimates propulsive force, particularly at high thrust.
2. The combination of X3D and Helios for Integrated 3-D CFD/CSD yields very good dynamic airloads predictions for the TRAM rotor. However, the steady normal force is over-predicted. The first four harmonics are accurate at low thrust. At high thrust 1, 2, and 4/rev airloads are well predicted, but 3/rev airloads are over-predicted.
3. Blade loads predictions capture general trends and peak-to-peak magnitude in flap bending moment, but miss higher frequency content, particularly at high thrust. Despite an over-prediction of 3/rev airloads at high thrust, blade loads under-predict the 3/rev flap bending moment.
4. Lag bending is well predicted at low thrust. A 2/rev component of lag bending seen in the experiment at high thrust is missed by the prediction.
5. Torsion moments are characterized by significant high frequency content, and this behavior is generally well predicted.
6. The 3-D stress field shows lower stress on the advancing side of the rotor and high stress from 270° to 0° azimuth, which is consistent with flap and lag bending moment patterns. Complex stress patterns are seen at the root of the blade assembly, with the pitch case under high stress and the flexbeam under low stress. The blade spar shows very high stress in the high thrust case, which may be due to an over-prediction of steady airloads or inaccurate material properties.

Future work is needed to understand the sources of discrepancies in blade loads extracted from X3D strains and those measured. The detailed 3-D stress results will be examined closely to see what information can be gained from them. Particular attention will be paid to dynamic stresses at the root of the blade assembly, which are critical for component design.

7. ACKNOWLEDGEMENTS

This work was performed at the University of Maryland Alfred Gessow Rotorcraft Center under Army Aeroflightdynamics Directorate funding through the Vertical Lift Research Center of Excellence (VLRCOE, grant number W911W61120012), with technical monitoring from Tom Maier and Roger Strawn. The authors would like to thank to William Warmbrodt and Larry Young (NASA Ames) for access to the TRAM drawings, Mark Potsdam (US Army) for the TRAM surface information, Wally Acree (NASA Ames) for the LCTR airfoil tables, Martin Annette (NASA Langley) for advice on materials modeling, and Wayne Johnson (NASA Ames) for advice and insight on the TRAM rotor. Finally, thanks to Byron Hanks and the rest of the Cubit development team at Sandia National Labs who aided in the meshing of the TRAM blade.

8. REFERENCES

[1] R. Strawn, "High-Performance Computing for Rotorcraft Modeling and Simulation," *Computing in Science and Engineering,* vol. 12, no. 5, pp. 27-35, Sep-Oct 2010.

[2] I. Fejtek and L. Roberts, "Navier-Stokes Computation of Wing/Rotor Interaction for a Tilt Rotor in Hover," *AIAA Journal,* vol. 30, no. 11, pp. 2595-2603, November 1992.

[3] R. Meakin, "Moving Body Overset Grid Methods for Complete Aircraft Tiltrotor Simulations," in *11th Computational Fluid Dynamics Conference, Fluid Dynamics and Co-located Conferences, AIAA Paper 3350*, Orlando, FL, 1993.

[4] M. Potsdam and R. Strawn, "CFD Simulations of Tiltrotor Configurations in Hover," *Journal of the American Helicopter Society,* vol. 50, no. 1, pp. 82-94, January 2005.

[5] N. Chaderjian and P. Buning, "High Resolution Navier-Stokes Simulation of Rotor Wakes," in *American Helicopter Society 67th Annual Forum Proceedings*, Virginia Beach, VA, May 3-5, 2011.

[6] A. M. Wissink, M. Potsdam, V. Sankaran, J. Sitaraman and D. Mavriplis, "A Dual-Mesh Unstructured Adaptive Cartesian Computational Fluid Dynamics Approach for Hover Prediction," *Journal of the American Helicopter Society,* vol. 61, no. 1, pp. 1-19, January 2016.

[7] W. E. Hall, "Prop-Rotor Stability at High Advance Ratios," *Journal of the American Helicopter Society,* vol. 11, no. 2, pp. 11-26, 1966.

[8] T. Gaffey, "The Effect of Positive Pitch-flap Coupling (Negative δ3) on Rotor Blade Motion Stability and Flapping," *Journal of the American Helicopter Society,* vol. 14, no. 2, pp. 49-67, 1969.

[9] W. Johnson, "Dynamics of Tilting Proprotor Aircraft in Cruise Flight," NASA TN D-7677, NASA Ames Research Center, 1974.

[10] V. Srinivas, I. Chopra and M. W. Nixon, "Aeroelastic Analysis of Advanced Geometry Tiltrotor Aircraft," *Journal of the American Helicopter Society,* vol. 43, no. 3, pp. 212-221, July 1998.

[11] M. W. Nixon, D. J. Piatak, L. M. Corso and D. A. Popelka, "Aeroelastic Tailoring for Stability Augmentation and Performance Enhancements of Tiltrotor Aircraft," *Journal of the American Helicopter Society,* vol. 45, no. 4, pp. 270-279, October 2000.

[12] C. W. Acree, "Effects of V-22 Blade Modifications on Whirl Flutter and Loads," *Journal of the American Helicopter Society,* vol. 50 , no. 3, pp. 269-278, July 2005.

[13] J. M. Bilger, R. L. Marr and A. Zahedi, "In-Flight Structural Dynamic Characteristics of the XV-15 Tilt Rotor Research Aircraft," *Journal of Aircraft,* vol. 19, no. 11, pp. 1005-1011, November 1982.

[14] J. J. Totah and J. F. I. Madden, "Rotor and Control System Loads Analysis of the XV-15 With the Advanced Technology Blades," NASA TM 102876, April 1991.

[15] W. Johnson, "Calculation of Tilt Rotor Aeroacoustic Model (TRAM DNW) Performance, Airloads, and Structural Loads," in *American Helicopter Society Aeromechanics Specialists' Meeting*, Atlanta, GA, November 13-15, 2000.

[16] W. Johnson, "Influence of Wake Models on Calculated Tiltrotor Aerodynamics," in *AHS Aerodynamics, Acoustics, and Test and Evaluation Technical Specialists' Meeting, San Francisco*, San Francisco, CA, January 23-25, 2002.

[17] A. Datta, M. Nixon and I. Chopra, "Review of Rotor Loads Prediction with the Emergence of Rotorcraft CFD," *Journal of the American Helicopter Society,* vol. 52, no. 4, pp. 287-317, October 2007.

[18] W. Johnson, "Milestones in Rotorcraft Aeromechanics," *Alexander A. Nikolsky Honorary Lecture, Journal of the American Helicopter Society,* vol. 56, no. 3, pp. 1-24, 2011.

[19] A. Datta, "X3D - A 3D Solid Finite Element Multibody Dynamic Analysis for Rotorcraft," in *American Helicopter Society Technical Meeting on Aeromechanics Design for Vertical Lift*, San Francisco, CA, January 20-22, 2016.

[20] A. Datta and W. Johnson, "Three-Dimensional Finite Element Formulation and Scalable Domain Decomposition for High Fidelity Rotor Dynamic Analysis," *Journal of the American Helicopter Society,* vol. 56, no. 2, pp. 1-14, July 2011.

[21] A. Datta and W. Johnson, "Integrated Aeromechanics with Three-Dimensional Solid-Multibody Structures," in *American Helicopter Society 70th Annual Forum Proceedings*, Montreal, QC, May 20-22, 2014.

[22] W. Staruk, I. Chopra and A. Datta, "Three-Dimensional CAD-Based Structural Modeling for Next Generation Rotor Dynamic Analysis," in *American Helicopter Society 70th Annual Forum Proceedings*, Montreal, QC, May 22-24, 2014.

[23] W. Staruk, E. Ward and I. Chopra, "CAD-Based 3-D Structural Dynamic Modeling of the Tilt Rotor Aeroacoustic Model (TRAM) Proprotor," in *American Helicopter Society 71st Annual Forum Proceedings*, Virginia Beach, VA, May 5-7, 2015.

[24] W. Staruk, I. Chopra and A. Datta, "Coupled Aerodynamics and 3-D Structural Dynamics of the Tilt Rotor Aeroacoustic Model (TRAM) Proprotor," in *AHS International Technical Meeting on Aeromechanics Design for Vertical Lift*, San Francisco, CA, Jan. 20-22, 2016.

[25] J. Sitaraman, M. Potsdam, A. Wissink, B. Jayaraman, D. Mavriplis and H. Saberi, "Rotor Loads Prediction Using Helios: A Multisolver Framework for Rotorcraft Aeromechanics," *Journal of Aircraft,* vol. 50, no. 2, pp. 478-492, March 2013.

[26] W. Carnegie, "Static Bending of Pre-twisted Cantilever Blading," *Proceedings of the Institution of Mechanical Engineers,* vol. 171, no. 1, pp. 879-894, 1957.

[27] D. Zupan and M. Saje, "On "A proposed standard set of problems to test finite element accuracy": the twisted beam," *Finite Elements in Analysis and Design,* vol. 40, pp. 1445-1451, 2004.

[28] L. A. Young, E. R. Booth, G. K. Yamauchi, G. Botha and S. Dawson, "Overview of the Testing of a Small-Scale Proprotor," in *American Helicopter Society 55th Annual Forum Proceedings*, Montreal, QC, Canada, May 25-27, 1999.

[29] Sandia National Laboratories, "CUBIT," [Online]. Available: https://cubit.sandia.gov/. [Accessed 30 10 2013].